International Journal of Thermal Sciences 50 (2011) 325–331

Contents lists available at ScienceDirect

International Journal of Thermal Sciences

journal homepage: www.elsevier.com/locate/ijts

3-D visualization of flow in microscale jet impingement systems

Yoonjin Won [a,*], Evelyn N. Wang [b], Kenneth E. Goodson [a], Thomas W. Kenny [a]

[a] Department of Mechanical Engineering, Stanford University, Stanford, CA 94305, USA
[b] Department of Mechanical Engineering, Massachusetts Institute of Technology, Cambridge, MA 02139, USA

ARTICLE INFO

Article history:
Received 2 February 2010
Received in revised form
7 August 2010
Accepted 7 August 2010
Available online 4 December 2010

Keywords:
Microjet
Impinging jet
Multi-jet
PIV, electronic cooling

ABSTRACT

Microjet impingement cooling devices promise high heat removal rates for the development of advanced thermal management solutions. However, understanding of microjet hydrodynamics is needed to optimize cooling performance. In this paper, we combined experiments and modeling to obtain three-dimensional (3-D) microjet flows. We fabricated single-jet and multi-jet arrays with 50 μm diameter orifices and used micron-resolution particle image velocimetry (μPIV) to capture two-dimensional (2-D) images of the flow field at different imaging planes. The data was subsequently used to obtain the out-of-plane (z-component) velocities, which play an important role in enhancing heat transfer at the impingement surface. The results from the reconstruction of the 3-D flow field offers new insights into the impact region of a single jet and optimized design of microjet cooling devices.

1. Introduction

Developing new cooling methods for electronic devices has become increasingly important due to the downsizing of electronic devices and the consequent increasing power densities. The first microscale cooling device prototype was developed and tested for integrated circuits (IC) cooling by Tuckerman and Pease [1]. Since their pioneering work, much research has been conducted on various types of liquid cooling devices. These devices, especially microchannels, are of great interest because of their relatively easy fabrication and compact size [2,3]. However, microchannels must overcome non-uniform temperatures due to the formation of dry-out regions and bubble blockage in two-phase cooling.

On a macroscale, jet cooling technologies have been traditionally used in large-scale industrial applications, such as metal manufacturing with high efficiencies [4,5]. The single-phase of macroscale jet ($d_{jet} > 1$ mm and $Re_d > 2000$), therefore, has been the subject of theoretical and experimental research activities [6,7]. For macroscale jets (d_{jet} of 0.79–6.35 mm), optimal orifice spacing was suggested to be $h/d_{jet} < 1$ to obtain highest heat transfer coefficients [8]. In addition, Li et al. tested single-phase submerged and confined jets and obtained heat transfer characteristics similar to those of free jets (d_{jet} of 1.59–12.7 mm, with Reynolds numbers of 4000–23,000, and orifice-to heat-source spicing of 1–5 jet diameters) [6]. Garimella and Rice achieved heat transfer coefficients of up to 6 W/cm^{2}K with a $Re_d = 23{,}000$ fluid [7]. Macroscale jets have been shown to achieve higher flux removal during fully-developed boiling [9]. During fully developed boiling, convective coefficients are not affected by surface conditions, subcooling, or velocity [10,9]. Since the insights into macroscale jets achieved are relevant to the performance of microscale jets, microjet impingement cooling ($d_{jet} < 1$ mm and $Re_d > 2000$) has been proposed as an alternative method to microchannels [11,12].

The study of microscale-confined liquid jets has the challenges of using multi-stacks of substrates and several bonding fabrication steps [13]. Thus, because of the similarity in their performances, microscale air jets have widely been studied instead of liquid jets. For example, Soon's simulation [14] reported 4.3 Watts of heat flux over a 1 cm^2 area with a single-jet with 76 μm diameter nozzle. His multi-jet array simulation addressed very low average surface temperature. Despite the challenges of liquid jets, we previously reported our fabrication of a compact, fabricated microscale jet system, which achieved a high heat flux removal rate of 40 W/cm^2 with $Q = 3.5$ ml/min [13,15]. However, to meet higher efficiency requirements, a better understanding of flow physics, in particular, 3-D flows is needed. The 3-D visualization of flow has been challenging due to the limited optical access of fabrication techniques. For example, a fabricated jet impingement device [15] has a top optical access and integrated heater with sensors at the bottom, and this heater led to an obstructed view.

In this paper, we designed, and tested single-jet and multi-jet devices for the flow visualization. In Section 1, we studied several impingement jet flow regimes and presented the designs and the fabrication process of the single-jet device. The fabricated device

* Corresponding author. Tel.: +1 650 714 1525; fax: +1 650 723 7657.
E-mail address: yoonjin@stanford.edu (Y. Won).

1290-0729/$ – see front matter © 2010 Elsevier Masson SAS. All rights reserved.
doi:10.1016/j.ijthermalsci.2010.08.005

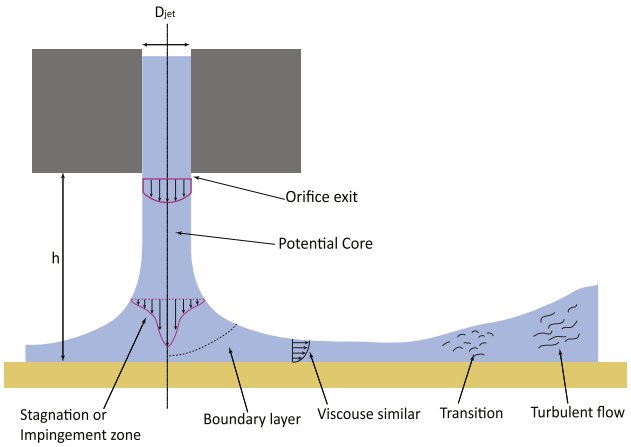

Fig. 1. Different regimes during the downstream development of an impinging jet.

has a bottom-side optical access, which enables us to efficiently collect flow images. Section 2 describes the experimental set up and the data extraction techniques using a micron-resolution particle image velocimetry (μPIV). Using μPIV, we obtained 2-D images for the study of the flow physics around the jet impingement. We then used the mass conservation to extract the out-of-plane velocity components [16]. The Results and Discussion section presents 2-D, and 3-D flow reconstructed images with different Reynolds numbers. This study not only provides insight into the flow physics in the jet impingement device, but also shows a promising cooling methodology to dissipate heat from electronic devices. The results enable us to understand the effective performance region of microjet impingement heat sinks for future study.

2. Designs and fabrication

2.1. Development of an impinging jet

Both theoretical and experimental studies of the flow fields of an impinging jet downstream have been researched to determine heat transfer rates [17,18]. The flow fields can be described using the different flow regimes, as depicted in Fig. 1. Because the flow physics and heat transfer coefficients are different in each regime, it is important to accurately predict the transitions between different regimes. The region where the jet impacts a wall is called the stagnation or impingement zone. The stagnation zone extends approximately to $0.7d_{jet}$, where d_{jet} is the diameter of the impinging jet. In this zone, the heat transfer coefficient is the largest and decreases in the radial direction. The downstream of the stagnation zone reaches the boundary layer region where the thickness of the boundary layer grows less than that of the liquid film. As the jet spreads radially outward, the thickness of the liquid film decreases initially, based on mass conservation principle, and then increases due to the slowing of the fluid caused by the viscous effects of the wall. At the same time, due to these viscous effects, the thickness of the boundary layer eventually equals that of the liquid film. This region is known as the viscous similar region. A similarity analysis can be used to derive the velocity profile in this region. Further downstream, the flow transitions to turbulence and then to a fully-developed turbulent flow, which is difficult to observe in a microscale liquid system because of the small Reynolds number of the flow [19,20].

2.2. Designs

Fig. 2 illustrates the simplified schematics of the microjet device used in this study. The impingement jet cooling system has one inlet (4 mm d_{inlet}) and four symmetrical outlets (2 mm d_{inlet}) at the corners to drive the working fluid. The single 50-μm diameter jet is located at the center. The h, the spacing between the jet orifice plate and the impingement surface, is 100 μm. The target cooling area is 1 cm × 1 cm, and the total area of the device is 2 cm × 2 cm. With this device, the water enters the top reservoir through the inlet at the top of the system at a constant flow rate and temperature (the ambient temperature of 298 K). It then passes through the jet orifice to the bottom reservoir, where it impinges on the upper surface of the glass substrate. The water travels laterally to the corners and exits through the four corner-outlets at the top of the system at a uniform pressure (atmosphere pressure). The top surface is considered a convective boundary condition with the insulation of entire exterior surfaces (Fig. 2b). Given the four outlets at the corners, the system can be analyzed as quad-symmetric. Although the four-outlet design enables the water to exit easily, the water still has several dead zones, which have relatively lower flows and heat removal rates.

2.3. Fabrication

We fabricated silicon microjets using conventional micromachining techniques. As illustrated in Fig. 3, the fabrication process

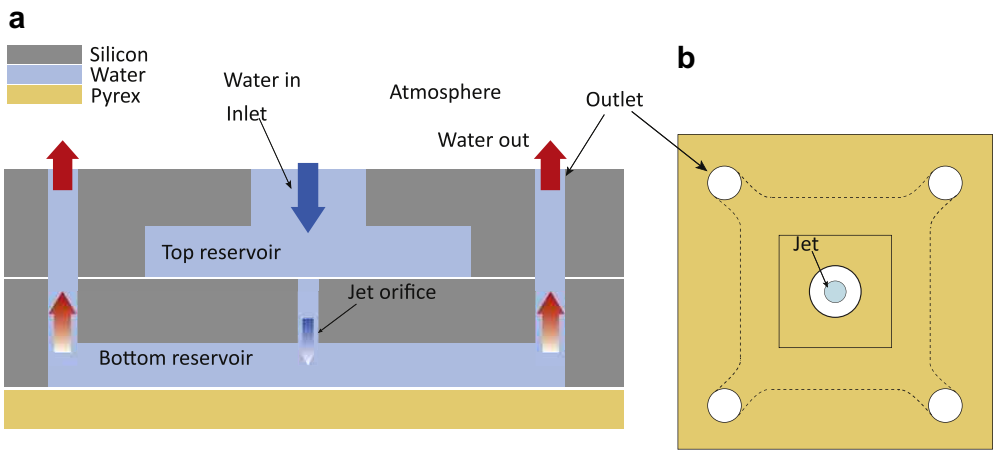

Fig. 2. Simplified schematics of the microjet device.

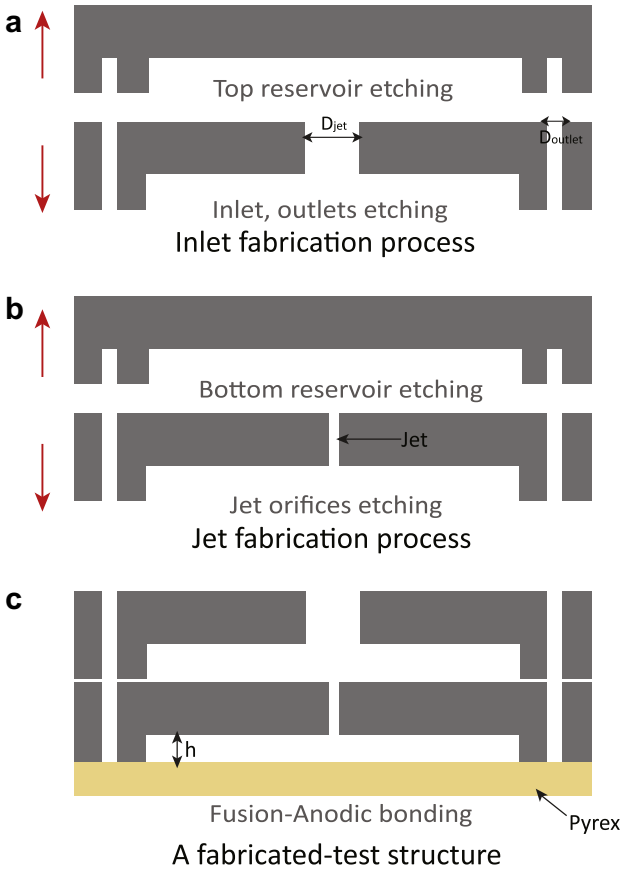

Fig. 3. Fabrication steps for a single microjet device and scheme of the device with (a) sideview and (b) topview.

consisted of two silicon wafers and a transparent substrate (Pyrex 7740). The top silicon substrate received a deep reactive ion etching (DRIE) from the front using a mask for an inlet and outlets and received another through-hole etching to delineate the top water reservoir and outlets from the backside. The second silicon substrate received a DRIE from the front using a mask for the jet orifices as well as another through-hole etching to delineate the bottom reservoir. The first wafer was fusion bonded to the second wafer, which was

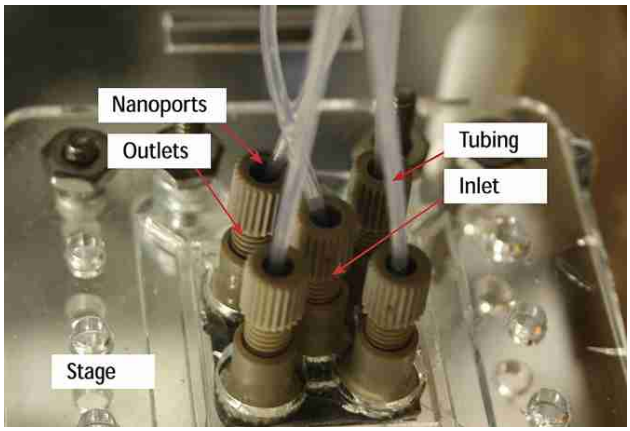

Fig. 4. Image of the front side of the device with fittings, including inlet and outlets. Total area of device is 2 cm × 2 cm. The cooling target area to be impinged by jets is 1 cm × 1 cm.

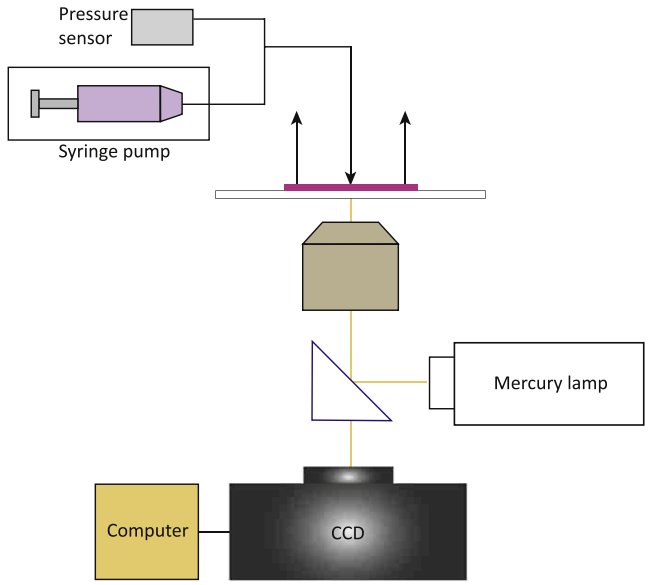

Fig. 5. Experimental set up.

then covered with a transparent substrate. This substrate enabled us to gain optical access to observe the jet impingement process. The multi-stacked substrates were then sliced into separate devices by mechanical sawing. Each resulting fabricated device has one inlet and four outlets. They are all connected with the commercial fittings (Upchurch Scientific N333 Nanoport™ assembly), with a diameter of 1.5875 mm. Fig. 4 presents a diced sample with fittings for the experiment.

3. Experimental set up and data extraction

3.1. Experimental set up

The experimental set up was designed to obtain velocimetry measurements for small Reynolds numbers and low flow rates of

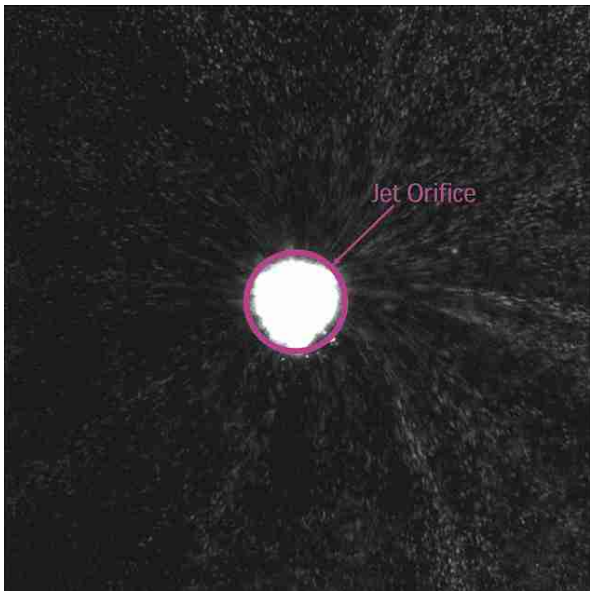

Fig. 6. Raw image of a 50 μm diameter water jet at 0.005 ml/min flow rate. The working fluid is seeded with fluorescent particles.

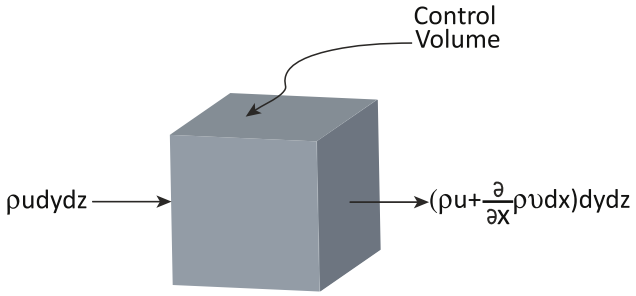

Fig. 7. Schematic work with a small control volume.

0.005 to 0.05 ml/min. As shown in Fig. 5, an epi-fluorescent microscope (Nikon Eclipse TE300) was used with illumination from a mercury lamp. The microscope is coupled to a CCD camera (Roper Scientific CoolSnap HQ) to obtain image pairs. For the μPIV images, the working fluid, DI water, was seeded with 1 μm diameter fluorescent particles to a volume density of 0.05%. To prevent the particle agglomeration, Triton-X surfactant (Sigma Corporation) was then added at a concentration of 0.005% by volume to the particle solution. The working fluid was provided by a syringe pump (Harvard), which was connected to the inlet of the device.

3.2. Data extraction for the 2-D flow construction using micron-resolution particle image velocimetry (μPIV)

Particle image velocimetry (PIV) is an optical method of fluid visualization that has been widely applied in investigating 2-D flow fields in microfluidic devices [21]. To prepare for the μPIV, the working fluid was seeded with fluorescent particles, where the particles were generally assumed to follow the flow dynamics. The motions of particles were observed and used to calculate velocity information. Using a CCD camera, we obtained pairs of images, which were captured from the bottom glass substrate, to which the device provided optical access. From these pairs of raw images, x, y, z-component velocities (u, v, w) were calculated. An example of a raw two-dimensional image of the jet flow captured by a CCD camera is presented in Fig. 6.

3.3. Data extraction for the 3-D flow construction

Without flow visualizations, we cannot fully understand the cooling performance of the impingement jet device. Compared to microchannel heat exchangers (primarily with in-plane flow), microjets exhibit large out-of-plane velocities; therefore, we need to visualize the three-dimensional (3-D) flow field in the device. Two-dimensional (2-D) slices at several focal depths were used to extract the out-of-plane velocity components from the law of mass conservation. Based on conservation theory, in a steady-state operation, the mass flow rate at the inlet and outlet are equal to the differential control volume (Fig. 7). For an incompressible flow, such as water, the density is constant. Therefore, we can simplify the equations by entering the mass term as $\rho u\,\mathrm{d}x\,\mathrm{d}y$. If the inlet mass flow to the left is known as ρu, the outlet mass flow from the right will be $\rho u + \frac{\partial}{\partial x}(\rho u)\mathrm{d}x$.

By capturing 2-D paired images, we can obtain u, (x-component velocity), v (y-component velocity), and calculate $\frac{\partial u}{\partial x}, \frac{\partial v}{\partial y}$ [19,16]. From Equations (1) and (2),

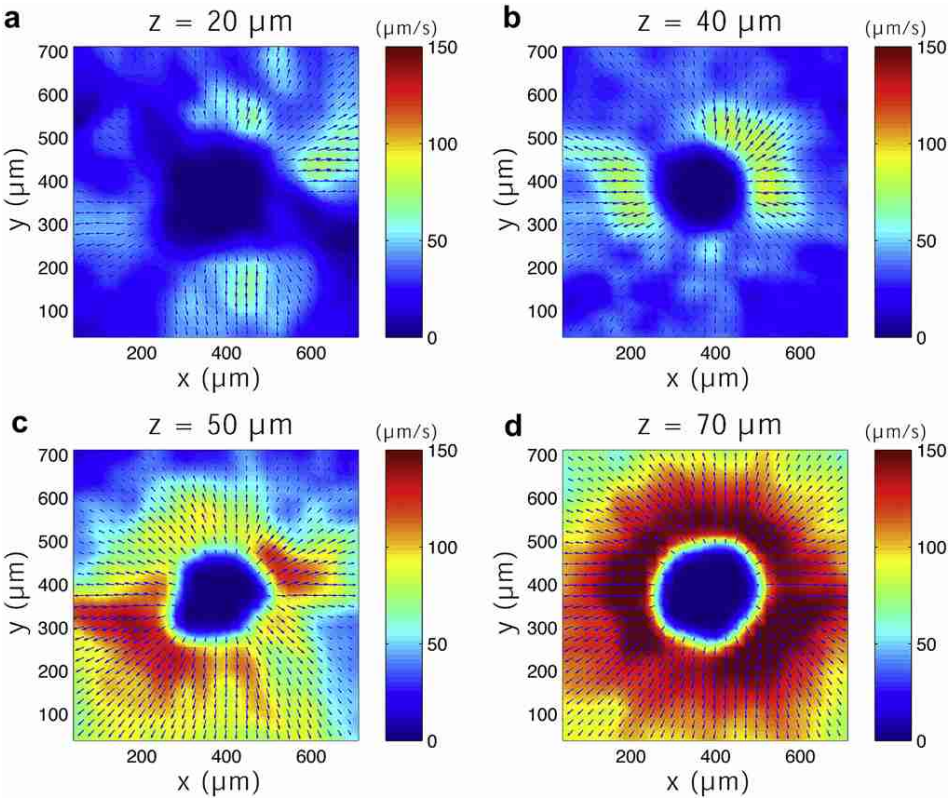

Fig. 8. 2-D μPIV velocity fields of a single-jet at (a) $z = 20$ μm (b) 40 μm (c) 50 μm (d) 70 μm: These velocity fields are radial symmetric, with the highest values near the impingement zone as expected.

$$(\text{Generation}) = (\text{Accumulation}) + (\text{out}) - (\text{in}) \quad (1)$$

$$\frac{\partial u}{\partial x} + \frac{\partial v}{\partial y} + \frac{\partial w}{\partial z} = 0 \quad (2)$$

By integrating Equation (2), w (z-component velocity) can be extracted:

$$w = \int \partial w = -\int \left(\frac{\partial u}{\partial x} + \frac{\partial v}{\partial y}\right) \partial z \quad (3)$$

The calculated values are used for the 3-D reconstruction in the Results and discussion section.

4. Results and discussion

4.1. Two-dimensional (2-D) flow

Fig. 8 compares the flow fields obtained from the 2-D μPIV experiment with a 50 μm diameter jet at (a) $z = 20$ μm, (b) 40 μm, (c) 50 μm, and (d) 70 μm locations with a 100 μm space between the impingement surface and the jet orifice plate. In a single micro-jet system, the flow around the impingement region gain is radially symmetric. The flow field around the jet is visualized by particles that follow the streamlines represented by arrows. These arrows present the absolute values of the x, y-velocities. In Fig. 8d, the streamlines around the jet indicate the fastest planar velocities, as illustrated by the arrows in the red background. However, the velocities decrease rapidly when the flows expand to the outlets, as illustrated by the arrows in the green area. These short velocity arrows in Fig. 8a and b are blue on a dark blue background. Because of the high number of concentrated particles in this region, the velocity fields close to the jet impingement zone could not be extracted from this μPIV work. With a single-jet, due to the heat received from the wall, the liquid temperature increases with the radial coordinates. The heat transfer coefficient decreases with the radial coordinates as a result of the increasing boundary layer thickness.

Fig. 9 compares the flow fields with a 50 μm-diameter, corner-jet of a multi-jet (5-jet) system. The corner-jet (a jet located closed to a corner-outlet) is at the center in this plot. Although other jets and corner-outlets are located outside the plot area, they affect the flow regimes in the plot. Therefore, it is important to know where they are located; other jets are beyond the right-bottom; one of corner-outlets, which has most effects on the flows, is beyond the left-top of the figure. Because of their locations, the water mainly flows from the right-bottom to left-top direction. The flows from the corner-jet and other jets converge at the corner and exit rapidly, as illustrated by the arrows in the red background. Thus, the water flows reduce the liquid temperature between the jet and the corner-outlet. At the same time, the flows towards the jet from the right-bottom side have the slow planar velocities, as illustrated by the arrows in the blue and dark blue background. These slow flows regimes are considered expanded stagnation regions between the impinged-jet and the flows from other jets. Therefore, to minimize the stagnation regions, multi-jet devices with additional outlets could be considered for the future design.

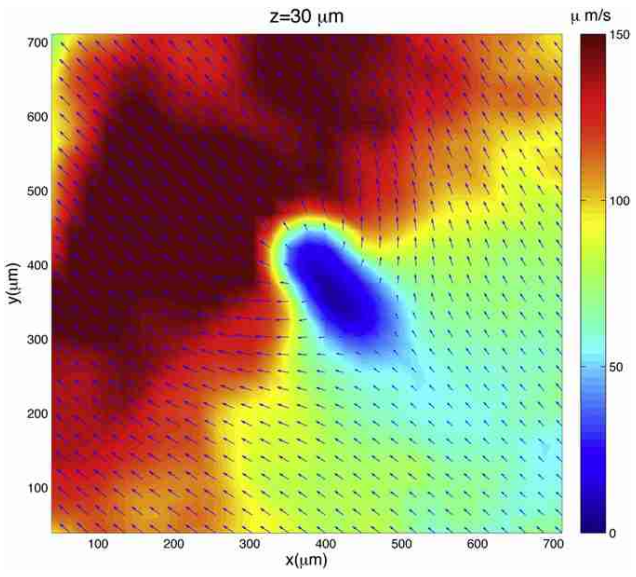

Fig. 9. 2-D μPIV velocity fields at of the corner jet of a multi-jet system at $z = 30$ μm.

4.2. Three-dimensional (3-D) flow

As shown in Fig. 10, we successfully reconstructed a 3-D flow for different Reynolds numbers (Fig. 10a,b has Reynolds number of 21, 63). After a jet exits the orifice plate, the z-component velocity forms rapidly at the jet orifice. As the focal depth decreases, the out-of-plane velocities also decelerate towards the bottom surface. The decelerated flow is influenced by the target surface to form the stagnation or the impingement zone. Outside of the impingement

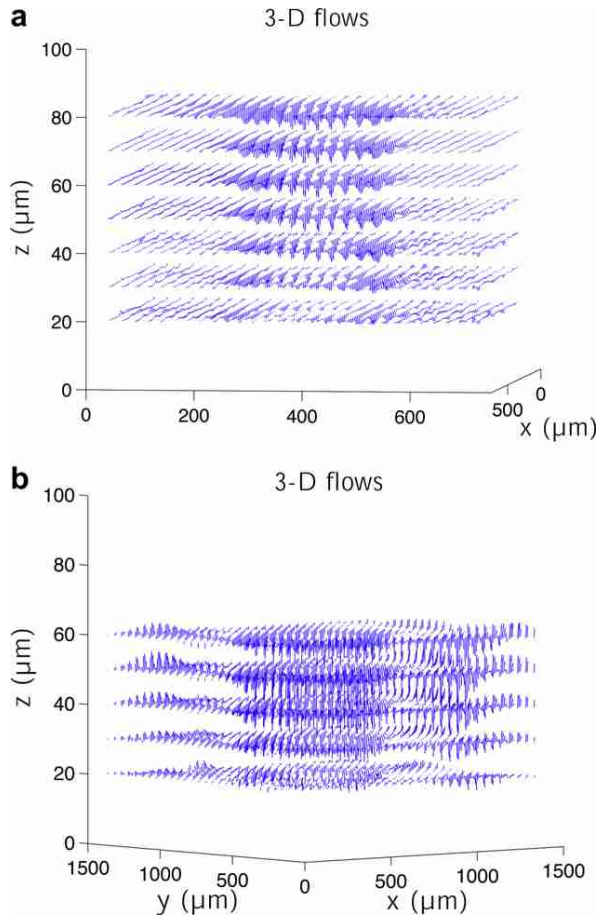

Fig. 10. 3-D Velocities at (a) $Re_d = 21$, (b) 63: Using Matlab code, out-of-plane velocities can be analyzed. With decreasing z, the out-of-plane velocities are reduced as the flows spread in the plane.

region, the out-of-plane velocities towards the top chamber form as a result of the increasing boundary layer thickness. The transverse (x, y) direction flow, known as the wall jet, is transformed to decelerate. The fluid eventually spreads outwards along the bottom glass substrate. The convective heat and mass transfer occur in both the stagnation and wall jet regions.

To observe normal z-direction velocities towards the top surface [22], beyond the impingement region, we extracted only out-of-plane velocities with positive z-component values at several focal depths of 20, 30, 40, 50, 60, 80 μm. As shown in Fig. 11 (Fig. 11a,b has Reynolds number of 21, 63) the impinged water accelerates in the thin-film disc region and decelerates through the jump. The positive velocities are induced around the central stream of impingement dissipating kinetic energy. The number of these velocity arrows increases as the impinging jet approaches the bottom surface. Very close to the bottom surface only a few flows will be formed because of the non-slip condition. In contrast to Fig. 11a, Fig. 11b presents higher our-of-plane velocities due to the higher Reynolds number, which leads to higher heat removal.

4.3. Velocity fields

Velocity fields have been studied because of the relation between velocities and heat transfer performance [23]. Averaged velocities, ($v_{avg} = (u^2 + v^2 + w^2)^{0.5}$) in the x-axis with standard deviations indicated by error bars for different focal depths, are illustrated in Fig. 12. At higher z-locations, close to the jet orifice plate, significantly higher z-direction velocities and relatively higher x, y-direction velocities can be seen.

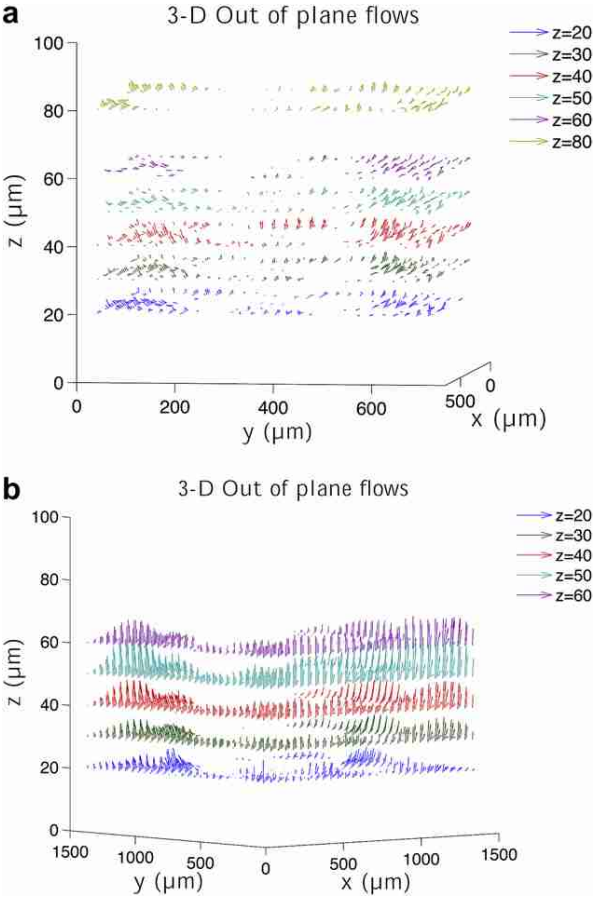

Fig. 11. Out-of-plane velocities at (a) $Re_d = 21$, (b) 63 with positive rates are shown in the z-direction at focal depths as 20, 30, 40, 50, 60, 80 μm. The size of the velocity factors increases as flows approach the bottom of the reservoir.

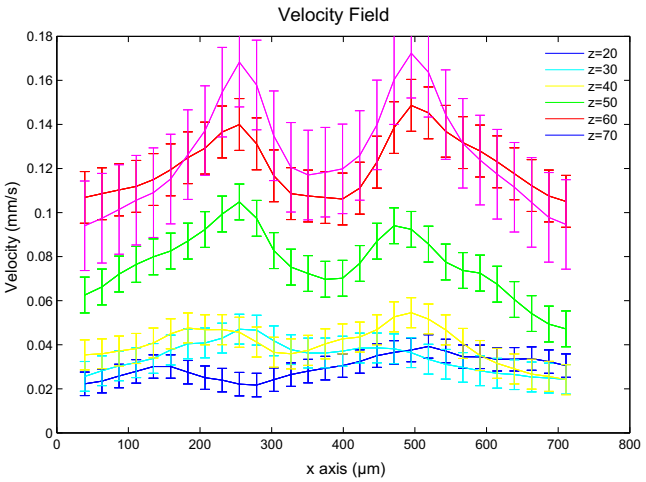

Fig. 12. Averaged velocity fields in the x-axis with standard deviations with different focal depths at $Re_d = 21$.

4.4. Benefits and drawbacks of the calculation

As explained in Experimental Set up Section, for the flow reconstruction, we applied the μPIV measurements using a CCD camera. The CCD camera was connected to a computer, which controlled the timing between image exposures and also permitted image pairs to be acquired at various times along the flow. With the μPIV measurement, the equipment did not disturb the real flow regimes. Thus, this measurement allowed us to obtain unobstructed flow velocities. For an accurate μPIV analysis, it is ideal if the average particle displacement of the region of interest corresponds to the camera speed. With a longer time interval, for example, the particles will travel further between frames. Therefore, it is difficult to identify which particles have to be convoluted to other particles. With a shorter time interval, it is difficult to identify the displacements of the particles with image pairs. Macroscale jets usually achieve high velocities and higher Reynolds numbers resulting in turbulence flows. In contrast to those jets, due to their small orifice sizes, microscale impinging jets achieve low velocities and low Reynolds numbers, resulting in a laminar flow and making it easy to use the μPIV techniques. When we operated at a relatively higher velocity, however, the CCD camera was limited to frame rates that can only corresponded to low flow rates. For further investigation of jet flow circulation, higher flow rates can be considered, but this would require a faster CCD camera.

5. Conclusions

Thermal management is one of the most essential components for the effective functioning of integrated circuit devices, for which typically lower temperatures can lead to better performance. To investigate the flow patterns for the enhanced heat transfer, we fabricated microscale impingement-jet devices with $D_{jet} = 50$ μm. The device obtained optical access from the bottom glass substrate, which sealed the impingement chamber. Under the condition of low Reynolds numbers ($Re_d = 21$–63), 2-D images were obtained at several focal planes and used to reconstruct the 3-D velocity fields. From the 3-D velocity fields that we obtained, we could quantify the flow physics around the impingement between the orifice and the bottom surface. Flow physics provide a better understanding of

heat removal because the heat transfer rates are correlated with flow physics. Our results thus give us insight into the effective region for the diameter, spacing and locations of a defined jet Future research should aim at developing test structures with multi-jet arrays and additional outlets to avoid flooding. Using the effective and stagnation regions from this work, the parameters of multi-jet devices can be optimized to achieve better performance. The optimization of design parameters will lead to improved designs of enclosed jet impingement coolers, engendering higher heat transfer rates in future designs for electronic circuit cooling.

Acknowledgments

This work is supported by MARCO IFC Program. This fabrication work was performed in part at the Stanford Nanofabrication Facility (a member of the National Nanotechnology Infrastructure Network) which is supported by the National Science Foundation under Grant ECS-9731293, its lab members, and the industrial members of the Stanford Center for Integrated Systems.

Nomenclature

d	orifice length [μm]
h	space between the top surface and the impingement surface [μm]
u	x-component velocity [m/s]
v	y-component velocity [m/s]
w	z-component velocity [m/s]
z	focal depths from the impingement surface [μm]
d_{inlet}	inlet diameter [μm]
d_{jet}	jet diameter [μm]
d_{outlet}	outlet diameter [μm]
Nu	Nusselts number
Q	flow rate [ml/min]
Re_{d}	Reynolds number at the jet exit
v_{avg}	averaged velocities [m/s]
v_{jet}	jet velocity [m/s]
μ	dynamic viscosity of the fluid [N s/m^2 or kg/m s]
ρ	density of the fluid [kg/m^3]

References

[1] D. Tuckerman, R. Pease, High-performance heat sinking for VLSI, IEEE, Electron Device Letters 2 (5) (1981) 126–129.
[2] A. Weisberg, H. Bau, J. Zemel, Analysis of microchannels for integrated cooling, International Journal of Heat and Mass 35 (10) (1992) 2465–2474.
[3] W. Qu, I. Mudawar, Experimental and numerical study of pressure drop and heat transfer in a single-phase micro-channel heat sink, International Journal of Heat and Mass Transfer 45 (2002) 2549–2565.
[4] M. Mazurkiewicz, Z. Kubala, J. Chow, Metal machining with high- pressure water-jet cooling assistance – a new possibility, Journal of Engineering for Industry 111 (1) (1989) 7–12.
[5] X. Luo, W. Chen, R. Sun, S. Liu, Experimental and numerical investigation of a microjet-based cooling system for high power LEDs, Heat Transfer Engineering 29 (9) (2008) 774–781.
[6] C. Li, S. Garimella, Prandtl-number effects and generalized correlations for confined and submerged jet impingement, International Journal of Heat and Mass Transfer 44 (18) (2001) 3471–3480.
[7] S. Garimella, R. Rice, Confined and submerged liquid jet impingement heat transfer, Journal of Heat Transfer 117 (1995) 871–877.
[8] S. Garimella, B. Nenaydykh, Nozzle-geometry effects in liquid jet impingement heat transfer, Journal of Heat and Mass Transfer 39 (14) (1996) 2915–2923.
[9] D. Wolf, F. Incropera, R. Viskanta, Local jet impingement boiling heat transfer, Journal of Heat and Mass Transfer 39 (7) (1996) 1395–1406.
[10] D. Wolf, F. Incropera, R. Viskanta, Jet Impingement Boiling, vol. 23, Academic Press, New York, 1993, pp. 1–132.
[11] A. Kiper, Impinging water jet cooling of vlsi circuits, International Communications in Heat and Mass Transfer 11 (1984) 517–526.
[12] Q. Lin, S. Wu, Y. Yuen, Y. Tai, MEMS impinging-jet cooling, Proceedings of ASME, 2000.
[13] E. Wang, J. Santiago, K. Goodson, T. Kenny, Microjet impingement cooling with phase change, Proceedings of ASME International Mechanical Engineering Congress and RD&D Expo, 2004.
[14] Y. Soon, N. Ghazali, Numerical simulation of a microchip cooling with microjet array, Jurnal Mekanikal 25 (2008) 39–49.
[15] E. Wang, L. Zhang, L. Jiang, J. Koo, J. Maveety, E. Sanchez, K. Good- son, T. Kenny, Micromachined jets for liquid impingement cooling of VLSI chips, Journal of Microelectromechanical Systems 13 (5) (2004) 833–842.
[16] E. Cummings, An image processing and optimal nonlinear filtering technique for particle image velocimetry of microflows, Experiments in Fluids (2000) 42–50.
[17] A. Pavlova, M. Amitay, Electronic cooling using synthetic jet impingement, Journal of Heat Transfer 128 (2006) 897–907.
[18] H. Fujimoto, N. Hatta, R. Viskanta, Numerical simulation of convective heat transfer to a radial free surface jet impinging on a hot solid, Heat and Mass Transfer 35 (4) (1999) 266–272.
[19] F.P. Incropera, D.P. DeWitt, Fundamentals of Heat and Mass Transfer. Wiley, 2007.
[20] S. Narumanchi, V. Hassani, D. Bharathan, Modeling single-phase and boiling liquid jet impingement cooling in power electronics, Technical Report (2005).
[21] E. Wang, S. Devasenathipathy, C. Hidrovo, D. Fogg, J. Koo, J. Santiago, K. Goodson, T. Kenny, A Quantitative Understanding of Transient Bubble Growth in Microchannels Using μPIV, Hilton Head (2004).
[22] E. Watson, The radial spread of a liquid jet over a horizontal plane, Journal of Fluid Mechanics Digital Archive 20 (03) (2006) 481–499.
[23] S. Whitaker, Forced convection heat transfer correlations for flow in pipes, past flat plates, single cylinders, single spheres, and for flow in packed beds and tube bundles, AIChE Journal 18 (2) (1972) 361–371.